Cluster nanoarchitecture and structural diversity of PIEZO1 in intact cells

Author list:

Clement Verkest[1], Lucas Roettger[1], Nadja Zeitzschel[1] & Stefan G. Lechner[1,*]

Affiliations:

[1] Department of Anesthesiology, University Medical Center Hamburg-Eppendorf, Germany

***Corresponding Author:**

Stefan G. Lechner

Department of Anesthesiology, University Medical Center Hamburg-Eppendorf

Martinistrasse 52, 20246 Hamburg, Germany

Phone: +49-(0)40-7410 53480

Email: s.lechner@uke.de

Abstract

The mechanically activated ion channel PIEZO1 confers mechanosensitivity to many cell types and is thus essential for numerous physiological processes triggered by mechanical cues[1–4]. PIEZO1 channels assemble as propeller-shaped trimers[5–7], which supposedly undergo a transition from a curved conformational state into a flattened state upon mechanical activation[8–11]. Whether this gating model also applies to PIEZO1 clusters and to what extent membrane curvature alters PIEZO1 conformation in living cells, is, however, still unclear. Here, we used MINFLUX nanoscopy to resolve the architecture of PIEZO1 clusters and demonstrate that PIEZO1 channels collectively deform the cell membrane into pit-shaped invaginations, which accommodate multiple channels and flatten in response to mechanical stimulation. Moreover, our data suggests that the deformability of the membrane and thus the conformation and sensitivity of PIEZO1 are altered by the architecture and the rigidity of the cytoskeleton. Together, our data provide previously unrecognized structural details about the subcellular distribution and the conformational variability of PIEZO1 in different cellular compartments, which challenge previously proposed hypotheses derived from studies of isolated channels and thus highlight the importance of examining PIEZO1 in its native environment, where additional factors contribute to channel function and structure.

Main text

PIEZO1 is a mechanosensitive ion channel that enables a variety of cell types to detect and respond to mechanical stimuli and is thus essential for numerous physiological processes[1,3,4,12,13]. PIEZO1 is a large protein consisting of more than 2500 amino acids per protomer (depending on the species) that forms a propeller-shaped homotrimer with a diameter of approximately 20 nm[5–7] (Fig. 1a). Studies utilizing high-speed atomic force microscopy, cryo-EM, patch-clamp electrophysiology as well as in-silico modelling[9,10,14–17], together suggested that the PIEZO blade domains are flexible and that PIEZO1 undergoes a transition from the bowl-shaped conformation into a flattened conformation upon activation[8,18]. The above-mentioned studies, however, only considered isolated channels, and thus it is still unclear if the proposed structural models and gating theories also apply to PIEZO1 channels in fully intact cells, where additional factors come into play. There is, for example, ample evidence suggesting that interactions between the membrane – and possibly the channel itself – with the cytoskeleton fine-tune the mechanosensitivity and thus possibly the conformation of PIEZO1[19–23]. Indeed, Mulhall et al. recently showed that PIEZO1 is more expanded in living cells than predicted by cryo-EM and provided evidence for channel flattening upon activation[11], though the mechanism causing the observed partial flattening remained elusive. Moreover, it is important to note, that although individual PIEZO1 channels can function as independent mechanosensors[2], numerous studies have shown that PIEZO1 channels form clusters in almost all cells, except red blood cells[24], both when expressed under the endogenous PIEZO1 promoter and when overexpressed in heterologous systems[21,25–33]. With regards to the functional relevance of PIEZO1 clusters, it was shown that clusters are recruited to focal adhesions[27], which are hotspots for mechanotransduction, where they supposedly mediate traction force-induced Ca^{2+} influx[29]. PIEZO1 clusters were also shown to be recruited to the rear end of keratinocytes where they control migration during wound healing and a recent study using a calcium indicator fused to the C-terminus of PIEZO1 showed that clusters mediate Ca^{2+}-influx in response to chemical and mechanical activation[32,33]. However, little is known about the nanoscale architecture of PIEZO1 clusters or the impact of clustering on channel conformation and function. Here, we thus set out to examine the three-dimensional architecture of PIEZO1 clusters as well as possible differences in the conformation of individual PIEZO1 channels in cellular compartments with different membrane curvature, using 3D-MINFLUX super-resolution microscopy in combination with DNA-PAINT (DNA-based point accumulation for imaging in nanoscale topography)[34–36] (Fig. 1a).

Nanoarchitecture of PIEZO1 clusters

To enable the detection and localization of individual PIEZO1 channels with MINFLUX/DNA-PAINT, we tagged PIEZO1 at the C-terminus with the green fluorescent protein

mGreenLantern (PIEZO1-mGL, Fig. 1a), which did not alter channel function with regards to mechanosensitivity, inactivation kinetics and single channel conductance, as evidenced by patch-clamp electrophysiology (Extended Data Fig. 1a-j). Consistent with previous reports [21,25–33], PIEZO1-mGL formed prominent clusters when expressed in N2a-P1KO cells[37], which were clearly discernible in confocal images (Fig. 1b) and efficiently detected by 3D-MINFLUX nanoscopy using a single domain nanobody (sd-Nb) directed against GFP that was conjugated to a DNA-PAINT docking strand (Fig. 1c). The MINFLUX raw localization data was post-processed as previously described (Extended Data Fig. 2a and references [36,38]), resulting in a final localization precision of 2.75 ± 0.91 nm, 2.86 ± 0.95 nm and 2.94 ± 1.15 nm along the x, y and z-axis, respectively (Fig. 1c). Importantly, in N2a cells transfected with PIEZO1-HA, only negligible background signals were detected in the MINFLUX scan (Extended Data Fig. 2b), demonstrating the specificity of anti-GFP sd-Nb and showing that freely diffusible or unspecifically bound imager strands do not confound the localization results.

The MINFLUX raw localizations did not only perfectly match the mGL fluorescence pattern obtained by confocal microscopy, but also revealed previously unrecognized structural details. The most peculiar feature was that PIEZO1 clusters appeared as ring-like structures in the 2D-projected MINFLUX data (Fig. 1c). Closer inspection of the raw localization data in 3D, revealed that all clusters exhibited significant expansion along the z-axis, with most clusters having a clearly recognizable pit-like shape, while others appeared to be spherical, vesicle-like objects (Fig. 1d-e and Supplementary Videos 1 and 2). To quantify the proportions of pit-shaped and spherical clusters, we segmented the raw MINFLUX localization data of each cluster into signals originating from the upper fifth (top) and the lower four fifth (bottom) (Fig. 1d), and classified clusters in which no channels were present near the center of the top segment (i.e. within a distance of 0.25 times the radius from the centroid), as pit-shaped clusters, whereas those clusters that did contain channels in this region were considered as spherical clusters (Fig. 1e). This classification scheme suggested that the great majority of the PIEZO1 clusters were pit-shaped (62.9%, 158 from 251), while only a small proportion appeared to be spherical in shape (93 from 251 clusters, Fig. 1f and g). To corroborate this finding, we generated a PIEZO1-mGL variant that carries an extracellular ALFA-tag at the distal end of the blade domain (PIEZO1-ALFA-mGL, Extended Data Fig. 3a), which did not alter channel function (Extended Data Fig. 3b-k), and quantified the proportion of PIEZO1 clusters that could be labelled with an anti-ALFA-Alexa-647 sd-Nb without permeabilization of the plasma membrane using total internal reflection (TIRF) microscopy (Extended Data Fig. 4a-d). In permeabilized cells anti-ALFA-Alexa-647 labelled almost all mGL-positive clusters (94.5 ± 5.5 %), whereas only 76.5 ± 12.7 % of the mGL-positive clusters were also Alexa647-positive in unpermeabilized cells, demonstrating that the great majority of PIEZO1 clusters are accessible from the extracellular side, which strongly supports the conclusion drawn from our

MINFLUX data, suggesting that approximately two thirds of the clusters form pit-shaped invaginations in the plasma membrane. We also examined the lateral mobility of PIEZO1 clusters in the cell membrane using live-cell TIRF imaging. Consistent with previous reports, we found that 66 ± 8 % of the clusters are immobile, while the remaining third exhibited significant lateral diffusion (Extended Data Fig. 4e, Supplementary Video 3). Considering the similarity of the proportions, it is tempting to speculate that the pit-shaped clusters detected by MINFLUX nanoscopy and the immobile clusters detected by live-cell TIRF imaging, represent the same population of clusters, but additional studies will be required to definitively address this question.

We next asked if pit-shaped PIEZO1 clusters change their shape in response to mechanical stimulation. To this end, we exposed PIEZO1-mGL-expressing N2a cells to a hypoosmotic solution (120 mOsm), which is well-known to activate PIEZO1, before fixation and compared cluster architectures from control cells with those from hypo-osmotically challenged cells. The most obvious effect of hypoosmotic stimulation was that the depth of pit-shaped clusters was significantly reduced from 144 ± 60.1 nm in control cells to 110.7 ± 54.8 nm in osmotically stimulated cells (Fig. 2a-c, Supplementary Videos 4 and 5, Extended Data Fig. 5). The proportions of pit-shaped and spherical clusters were unchanged, but interestingly, there was a slight decrease in the average number of channels per cluster (Fig. 2d and e). There was also a small increase in the pit opening radius, which was, however, not statistically significant (control: 72.8 ± 27.33 vs. osmo: 78.4 ± 31.1 nm, mean ± SD, Fig. 2f). Considering that PIEZO1 is thought to be activated by changes in membrane curvature and considering further that pit-shaped invaginations exhibit a strong gradient of curvatures ranging from positive values (concave) at the bottom to negative values (convex) at the pit opening (Fig. 2b), small changes in cluster structure or in the relative localization of channels within the pits, could have large effects on the curvature that individual channels are exposed to and hence on their activity. We thus fitted the surface of the clusters and calculated the gaussian curvature of the surface at the coordinates where individual channels were detected. This analysis revealed that the mean curvature that individual channels are exposed to, is significantly reduced during hypoosmotic stimulation and that more channels are exposed to negative curvatures (Fig. 2g). Hence, together our data suggest that PIEZO1 channels collectively deform the membrane into large pit-shaped invaginations that change their shape in response to mechanical stimulation resulting in significant changes in local curvature and thus possibly activation of individual channels.

Conformational diversity of PIEZO1

PIEZO1 undergoes a transition from the curved (bowl-shaped) conformation into a flattened conformation upon mechanical activation[4,8,11,18], which involves tilting and counterclockwise

(viewed from above) rotation of the blades such that the distance between the distal ends of the blades (interblade distance) increases by ~8 nm in the fully flattened conformation [9] (Fig. 3a). To examine if, and to what extent, differences in basal membrane curvature can alter the conformation if individual PIEZO1 channels in different cellular compartments, we next compared the interblade distances of trimers located at the flat interface between the soma and the substrate with those of trimers located in highly curved neurites (Fig. 3b, Extended Data Fig. 6 and Supplementary Videos 6-10). To this end we performed MINFLUX imaging with a single domain nanobody directed against the ALFA-tag (Extended Data Fig. 7) that was inserted at the distal end of the PIEZO1 blade domain and measured the distances between ALFA-tag localizations in triple-labelled PIEZO1 trimers (Fig. 3a). Localization traces originating from triple-labelled PIEZO1 trimers were identified by searching for three adjacent traces that were less than 40 nm apart, which we assumed is the maximum distance two Atto-655 molecules bound to the same PIEZO1 trimer can possibly have, and that had no other neighboring traces within a distance of 60 nm (Extended Data Fig. 8a). Using these identification criteria, we detected 67 trimers that were located at the cell soma and 30 trimers that resided in neurites (Figure 3c and Extended Data Fig. 9a-d). The mean localization errors of the MINFLUX traces were approximately 4 nm in all three dimensions (Extended Data Fig. 9a), which was almost an order of magnitude smaller than the expected interblade distance. We next aligned the localization trace means of each trimer to a two-dimensional reference trimer (i.e. an equilateral triangle with a side length of 25 nm) using an iterative closest point algorithm and plotted the overlays of all aligned trimers found in somata and neurites (Fig. 3e). Interestingly, the mean localization clouds in these overlays were not spherical but slightly elongated in direction away from the trimer center, indicating that the variability does not only result from the isotropic MINFLUX localization error (Fig. 3d), but also reflects varying degrees of PIEZO1 flattening. We also found that the interblade angles (the angles between the lines connecting the distal ends of the blades; Fig 3a), while being normally distributed around 60°, showed notable variability (Extended Data Fig. 9b), indicating additional rotational flexibility of the distal blades, as previously reported[11]. Most importantly, however, our data showed that the mean interblade distances of trimers found in somata were significantly larger than the interblade distances of trimers residing in neurites (soma: 23.9 ± 5.1 nm, N=67 vs. neurite: 19.8 ± 5.1 nm, N=30, P=0.00019, Student's T-test; Fig. 3e), which was exactly the opposite of what we had expected, considering the high positive curvature of the neurites. To ensure that our results were not confounded by false positive trimers – i.e. trace triplets that do not originate from a single triple-labelled trimer but from two adjacent yet partially labelled trimers – we refined the analysis using more stringent cutoff criteria for trimer identification. However, we obtained the same results over a wide range of cutoff values (Extended Data Fig. 8b and c), supporting our original observation that PIEZO1 trimers are more contracted in neurites as

compared to the cell soma. Interestingly, there was also no correlation between interblade distances and neurite diameters, which ranged from 253 nm to 2308 nm (Fig. 3f). Together, these data suggest that highly convex membrane curvature does not flatten PIEZO1 (Fig. 3g), which may seem counterintuitive at first glance. However, it is important to note that the membrane is tightly attached to the cytoskeleton and thus the extent to which PIEZO1 deforms the membrane – and thus its own conformation – may not only depend on the membrane bending modulus (a measure for the tendency of the membrane to oppose bending) and on membrane curvature, but possibly also on the rigidity of the underlying cytoskeleton and on the density of membrane-cytoskeleton attachments (Fig. 4a). To test this hypothesis, we next asked if disruption of the cytoskeleton with the actin polymerization inhibitor cytochalasin-D (cyto-D) alters the conformation of PIEZO1. Consistent with previous reports, incubation of N2a-cells with 2 µM cyto-D significantly increased the peak current amplitudes of PIEZO1-mediated currents in pressure-clamp recordings and shifted the pressure-response curve to less negative pressures (-40.5 ± 11.3 mmHg to -29.1 ± 10.5 mmHg, Fig. 4b and c). To examine if this increase in mechanosensitivity was accompanied by conformational changes, we next compared the interblade distances of PIEZO1 trimers from cyto-D-treated cells with those from control cells. To rule out a possible confounding effect caused by subtle differences in membrane curvature, we only considered PIEZO1 trimers that were located at the cell-substrate interfaces, which were completely flat in both conditions (Fig. 4d). Strikingly, PIEZO1 trimers detected in cyto-D treated cells had significantly smaller interblade distances (control: 23.9 ± 5.1 nm vs. cyto-D: 20.6 ± 5.3 nm), demonstrating that PIEZO1 is more contracted and causes a stronger deformation of the membrane in the absence of a cytoskeletal support structure (Fig. 4e-g and Extended Data Fig. 9e).

Together, our data show, that PIEZO1 conformation at rest is not solely controlled by membrane curvature and suggest that the architecture and rigidity of the underlying cytoskeleton plays a more important role.

Discussion

In this study we resolved the three-dimensional architecture of PIEZO1 clusters with a spatial resolution of less than 3 nm using MINFLUX nanoscopy, which revealed that PIEZO1 channels collectively deform the membrane into pit-shaped invaginations that change their shape in response to mechanical stimulation resulting in significant changes in local curvature and thus possibly activation of individual channels. Moreover, we measured the intramolecular distances between the blades of individual PIEZO1 trimers and found that PIEZO1 conformation at rest is strongly influenced by the architecture and rigidity of the cytoskeleton.

While it is well-acknowledged that PIEZO1 channels form clusters in living cells, only little is known about the relevance of these clusters for cellular mechanosensitivity, their nanoscale architecture and not least the impact of clustering on channel conformation and function. Regarding the latter, modelling studies suggested that individual PIEZO1 channels deform the membrane far beyond its perimeter, because a sharp transition from the curved PIEZO dome to a flat membrane would come at a higher energetic cost, such that the total membrane footprint of individual PIEZO1 channels is much bigger than the channel itself and can reach up to ~5,000 nm^2 [8,16]. Accordingly, with regards to PIEZO1 clustering it has been proposed that the opposing curvatures of the membrane footprints of two nearby channels would create an energetic constraint in the interjacent membrane such that nearby channels would either repel each other or induce mutual flattening to reduce the overall energy of the system[8,17,39]. Here we show that this does not seem to be the case and that PIEZO1 channels instead collectively deform the membrane into large pit-shaped invaginations that accommodate up to twenty channels and more. We cannot rule out that additional membrane-bending proteins are required for pit formation, but considering that PIEZO1 appears to exert a strong bending force onto membranes [9,10,16], it seems likely that pit formation provides an effective mechanism to minimize the energy of the PIEZO1 cluster system, because the membrane footprints of individual PIEZOs can seamlessly integrate into the overall pit curvature without causing energetic constraints in the membrane between neighboring channels PIEZOs. This hypothesis is supported by recent studies showing that PIEZO1 accumulates in concave environments such as the dimple regions of red blood cells[24] and in invaginations formed by cells grown on nanobars[40]. Regarding the effect of clustering on PIEZO1 function, we have not tested if PIEZO1 channels that are located in clusters are more sensitive than individual channels, because currently available imaging techniques lack the spatial resolution and the sensitivity to test this hypothesis. Moreover, due to the high channel density the algorithm that we used to identify triple labelled PIEZO1 trimers, which uses very stringent cutoff criteria to prevent the detection of false positives (Extended Data Fig. 8a), failed to identify trimers within clusters such that we could not assess conformational variability of PIEZO1 within clusters. However, considering that pit-shaped invaginations create a microenvironment that exhibits a strong gradient of curvatures, with highly positive curvatures at the bottom and negative curvatures close to the pit opening, it is nevertheless tempting to speculate that clusters may serve as hotspots for mechanosensitivity where subtle changes in the pit shape and in the relative position of the channels within the pit have strong effects on channel activity. The strong local deformation of the membrane by multiple PIEZO1 channels also raises the question if PIEZO1 channels may have a function beyond mechanosensitivity. Indeed, recent studies have shown that Piezo inhibits axon regeneration and dendrite targeting in Drosophila and suggested that it might do so independent of its mechanosensitivity[41,42]. Although it is

conceivable that the membrane footprint of individual PIEZO1 channels might be sufficient to prevent the formation of protrusions that ultimately form filopodia and neurites, the collective deformation of the membrane by multiple PIEZO1 channels that was observed here would probably be way more effective.

The second major observation of our study was that PIEZO1 channels in highly curved neurites were more contracted than channels located at the flat interface between the cell soma and the substrate (Fig. 3g), demonstrating that PIEZO1 conformation at rest can differ between cellular compartments. Given the ample evidence from studies examining PIEZO1 reconstituted in lipid vesicles, which showed that positive membrane curvature significantly flattens the channel[9,10], this observation might appear counterintuitive at first glance. However, in living cells, additional factors that can control PIEZO1 conformation come into play. Thus, the cell membrane is tightly coupled to the underlying cytoskeleton via membrane cortex attachments, which can prevent lateral membrane flow[43] and have been proposed to impose constraints on the size of PIEZO1s membrane footprint[8,16] – i.e. the degree of PIEZO1 flattening. Importantly, it is well-established that the spacing of such membrane attachments and the overall architecture of the cytoskeleton are significantly different in the cell soma as compared to axons and neurite[44–46], which could explain differences in channel flattening between the two compartments. Indeed, we found that disruption of the cytoskeleton with cyto-D significantly reduces PIEZO1 interblade distances without changing membrane curvature (Fig. 4). Most importantly, our data shows that despite being more contracted after cyto-D treatment (Fig. 4 e-g), PIEZO1 is more sensitive to mechanical stimuli (Fig. 4b and c), which challenges previously proposed theories suggesting that sensitization of PIEZO1, e.g. by the chemical activator Yoda1, requires partial channel flattening[47].

In summary, our data provide novel insights into the subcellular distribution and the conformational variability of PIEZO1 in different cellular compartments, which challenge previously proposed hypotheses derived from studies of isolated channels and highlight the importance of examining PIEZO1 in its native environment, where additional factors contribute to channel function and structure.

References

1. Szczot, M., Nickolls, A. R., Lam, R. M. & Chesler, A. T. The Form and Function of PIEZO2. *Annu Rev Biochem* **90**, 507–534 (2021).
2. Lewis, A. H. & Grandl, J. Piezo1 ion channels inherently function as independent mechanotransducers. *Elife* **10**, e70988 (2021).
3. Kefauver, J. M., Ward, A. B. & Patapoutian, A. Discoveries in structure and physiology of mechanically activated ion channels. *Nature* **587**, 567–576 (2020).

4. Xiao, B. Mechanisms of mechanotransduction and physiological roles of PIEZO channels. *Nat Rev Mol Cell Biol* **25**, 886–903 (2024).
5. Saotome, K. *et al.* Structure of the mechanically activated ion channel Piezo1. *Nature* (2017) doi:10.1038/nature25453.
6. Guo, Y. R. & MacKinnon, R. Structure-based membrane dome mechanism for Piezo mechanosensitivity. *eLife Sciences* **6**, e33660 (2017).
7. Zhao, Q. *et al.* Structure and mechanogating mechanism of the Piezo1 channel. *Nature* (2018) doi:10.1038/nature25743.
8. Young, M., Lewis, A. H. & Grandl, J. Physics of mechanotransduction by Piezo ion channels. *Journal of General Physiology* **154**, e202113044 (2022).
9. Yang, X. *et al.* Structure deformation and curvature sensing of PIEZO1 in lipid membranes. *Nature* **604**, 1–7 (2022).
10. Lin, Y.-C. *et al.* Force-induced conformational changes in PIEZO1. *Nature* **573**, 230–234 (2019).
11. Mulhall, E. M. *et al.* Direct observation of the conformational states of PIEZO1. *Nature* **620**, 1117–1125 (2023).
12. Wu, J., Lewis, A. H. & Grandl, J. Touch, Tension, and Transduction – The Function and Regulation of Piezo Ion Channels. *Trends in Biochemical Sciences* **42**, 57–71 (2017).
13. Ridone, P., Vassalli, M. & Martinac, B. Piezo1 mechanosensitive channels: what are they and why are they important. *Biophys Rev* **11**, 795–805 (2019).
14. Lewis, A. H. & Grandl, J. Inactivation Kinetics and Mechanical Gating of Piezo1 Ion Channels Depend on Subdomains within the Cap. *Cell Rep* **30**, 870-880.e2 (2020).
15. Wang, Y. *et al.* A lever-like transduction pathway for long-distance chemical- and mechano-gating of the mechanosensitive Piezo1 channel. *Nature Communications* **9**, 1300 (2018).
16. Haselwandter, C. A., Guo, Y. R., Fu, Z. & MacKinnon, R. Quantitative prediction and measurement of Piezo's membrane footprint. *Proceedings of the National Academy of Sciences of the United States of America* **119**, e2208027119 (2022).
17. Haselwandter, C. A. & MacKinnon, R. Piezo's membrane footprint and its contribution to mechanosensitivity. *eLife* **7**, e41968 (2018).
18. Verkest, C. & Lechner, S. G. Advances and recent insights into the gating mechanisms of the mechanically activated ion channels PIEZO1 and PIEZO2. *Current Opinion in Physiology* **31**, 100625 (2023).
19. Gottlieb, P. A., Bae, C. & Sachs, F. Gating the mechanical channel Piezo1: a comparison between whole-cell and patch recording. *Channels (Austin)* **6**, 282–289 (2012).
20. Cox, C. D. *et al.* Removal of the mechanoprotective influence of the cytoskeleton reveals PIEZO1 is gated by bilayer tension. *Nature Communications* **7**, 10366 (2016).

21. Verkest, C. *et al.* Intrinsically disordered intracellular domains control key features of the mechanically-gated ion channel PIEZO2. *Nat Commun* **13**, 1365 (2022).
22. Wang, H. J. *et al.* Microscale geometrical modulation of PIEZO1 mediated mechanosensing through cytoskeletal redistribution. *Nat Commun* **15**, 5521 (2024).
23. Wang, J. *et al.* Tethering Piezo channels to the actin cytoskeleton for mechanogating via the cadherin-β-catenin mechanotransduction complex. *Cell Reports* **38**, 110342 (2022).
24. Vaisey, G., Banerjee, P., North, A. J., Haselwandter, C. A. & MacKinnon, R. Piezo1 as a force-through-membrane sensor in red blood cells. *Elife* **11**, e82621 (2022).
25. Chen, X. *et al.* A Feedforward Mechanism Mediated by Mechanosensitive Ion Channel PIEZO1 and Tissue Mechanics Promotes Glioma Aggression. *Neuron* **100**, 799-815.e7 (2018).
26. Ridone, P. *et al.* Disruption of membrane cholesterol organization impairs the activity of PIEZO1 channel clusters. *J Gen Physiol* **152**, e201912515 (2020).
27. Yao, M. *et al.* Force- and cell state-dependent recruitment of Piezo1 drives focal adhesion dynamics and calcium entry. *Sci Adv* **8**, eabo1461 (2022).
28. Hu, J. *et al.* Microglial Piezo1 senses Aβ fibril stiffness to restrict Alzheimer's disease. *Neuron* **111**, 15-29.e8 (2023).
29. Ellefsen, K. L. *et al.* Myosin-II mediated traction forces evoke localized Piezo1-dependent Ca 2+ flickers. *Commun Biol* **2**, 1–13 (2019).
30. Shin, S. M. *et al.* Peripheral sensory neurons and non-neuronal cells express functional Piezo1 channels. *Mol Pain* **19**, 17448069231174315 (2023).
31. Yu, Z.-Y. *et al.* Piezo1 is the cardiac mechanosensor that initiates the cardiomyocyte hypertrophic response to pressure overload in adult mice. *Nature Cardiovascular Research* **1**, 577 (2022).
32. Holt, J. R. *et al.* Spatiotemporal dynamics of PIEZO1 localization controls keratinocyte migration during wound healing. *Elife* **10**, e65415 (2021).
33. Bertaccini, G. A. *et al.* Visualizing PIEZO1 Localization and Activity in hiPSC-Derived Single Cells and Organoids with HaloTag Technology. 2023.12.22.573117 Preprint at https://doi.org/10.1101/2023.12.22.573117 (2024).
34. Balzarotti, F. *et al.* Nanometer resolution imaging and tracking of fluorescent molecules with minimal photon fluxes. *Science* **355**, 606–612 (2017).
35. Gwosch, K. C. *et al.* MINFLUX nanoscopy delivers 3D multicolor nanometer resolution in cells. *Nat Methods* **17**, 217–224 (2020).
36. Ostersehlt, L. M. *et al.* DNA-PAINT MINFLUX nanoscopy. *Nat Methods* **19**, 1072–1075 (2022).

37. Moroni, M., Servin-Vences, M. R., Fleischer, R., Sánchez-Carranza, O. & Lewin, G. R. Voltage gating of mechanosensitive PIEZO channels. *Nature Communications* **9**, 1096 (2018).
38. Sahl, S. J. *et al.* Direct optical measurement of intramolecular distances with angstrom precision. *Science* **386**, 180–187 (2024).
39. Jiang, W. *et al.* Crowding-induced opening of the mechanosensitive Piezo1 channel in silico. *Commun Biol* **4**, 84 (2021).
40. Yang, S. *et al.* Membrane curvature governs the distribution of Piezo1 in live cells. *Nat Commun* **13**, 7467 (2022).
41. Song, Y. *et al.* The Mechanosensitive Ion Channel Piezo Inhibits Axon Regeneration. *Neuron* **102**, 373-389.e6 (2019).
42. Xie, Q. *et al.* Transcription factor Acj6 controls dendrite targeting via a combinatorial cell-surface code. *Neuron* **110**, 2299-2314.e8 (2022).
43. Shi, Z., Graber, Z. T., Baumgart, T., Stone, H. A. & Cohen, A. E. Cell Membranes Resist Flow. *Cell* **175**, 1769-1779.e13 (2018).
44. Xu, K., Zhong, G. & Zhuang, X. Actin, spectrin, and associated proteins form a periodic cytoskeletal structure in axons. *Science* **339**, 452–456 (2013).
45. He, J. *et al.* Prevalent presence of periodic actin-spectrin-based membrane skeleton in a broad range of neuronal cell types and animal species. *Proc Natl Acad Sci U S A* **113**, 6029–6034 (2016).
46. Svitkina, T. M. Actin Cell Cortex: Structure and Molecular Organization. *Trends Cell Biol* **30**, 556–565 (2020).
47. Botello-Smith, W. M. *et al.* A mechanism for the activation of the mechanosensitive Piezo1 channel by the small molecule Yoda1. *Nature communications* **10**, 4503 (2019).

Methods

Generation of PIEZO constructs

A mouse PIEZO1-IRES-GFP plasmid (Addgene #80925) was used as the initial template to generate most of the constructs of the present work, using a similar strategy described in earlier studies [21,48]. PIEZO1-mGreenLantern fusion protein (PIEZO1-mGL) was generated by amplifying the coding sequence of the green fluorescent protein mGreenLantern[49] from a LifeAct-mGreenLantern plasmid (git from G. Petsko, Addgene #164459), and inserted with a SG linker after the C-ter of PIEZO1 plasmid, where the IRES-GFP has sequence has been excised beforehand by PCR. The PIEZO1-ALFA-IRES-GFP construct was generated by inserting a synthetic DNA fragment coding for amino acid 1 to 180 of mouse PIEZO1, with the

ALFA tag sequence inserted after amino acid position H86 and flanked by one proline on each side (GeneArt Custom Gene Synthesis, ThermoFisher)[50] , into a PIEZO1-IRES-GFP plasmid excised for the corresponding 1-180 coding region. A plasmid version of PIEZO1-ALFA without the IRES-GFP sequence but with a C-ter HA-tag was also generated. The PIEZO1-ALFA-IRES-GFP plasmid was later used as a template to generate the PIEZO1-ALFA-mGreenLantern (PIEZO1-ALFA-mGL), by exchanging the IRES-GFP sequence with mGreenLantern, as described above. All DNA fragments were generated by PCR (primers from Sigma) using KAPA HiFi polymerase (Roche) and cloning was performed with homologous recombination (Gibson Assembly, NEBuilder HiFi, New England Biolabs). PCR reactions were digested with DpnI (New England Biolabs, 37°C, 1h) and column purified with standard kits (NucleoSpin from Macherey-Nagel or PureLink from Invitrogen) before being assembled by homologous recombination and then transformed in electrocompetent Stbl4 or Dh5a bacteria (Invitrogen) and grown at 30°C for 48h (Stbl4) or 37°C overnight (Dh5a). Selected clones were entirely sequenced (Eurofins) to ensure that no mutation was present.

Cell culture

Mouse neuroblastoma Neuro-2a PIEZO1-Knockout cell line (N2A-P1KO) was generated and characterized previously from Neuro-2a ATCC CCL-131 (a gift from G.R Lewin[37]). Cells were grown in Dulbecco's Modified Eagle Medium (DMEM) and optimal Minimal Essential Medium (opti-MEM) (1:1 mixture), supplemented with 10% Fetal Bovine Serum, 2mM L-glutamine and 1% peniciline/streptomycine (all from ThermoFisher). For live TIRF imaging experiments, DMEM and opti-MEM medium without phenol red were used. N2A-P1KO cells were cultured at 37°C with 5% CO2. Cells were seeded on poly-L-lysine (PLL, Sigma) coated and methanol- and acid-washed glass coverslips (12mm diameter for patch-clamp recordings, #1.5 and 18mm diameter for Minflux and TIRF imaging on fixed samples), or PLL-coated 35mm glass-bottom dishes (MatTek High Precision #1.5 Coverslip, TIRF microscopy live-imaging). N2A-P1KO cells were transfected one or two days after plating using polyethylenimine (PEI, Linear PEI 25K, Polysciences). For one 12mm coverslip, 7µl of a 360µg/ml PEI solution is mixed with 9µl PBS. Plasmid DNA is diluted in 20µl PBS (0.6 µg/coverslip) and then the 16µl PEI-PBS solution is added to the DNA solution. After at least 10 minutes of incubation, the DNA-PEI mix is added drop by drop and mixed by gentle swirling. For a 35mm dish or 18mm coverslip, 2.0µg DNA is used and PBS/PEI volumes are adjusted accordingly. 24h later, the medium is replaced by fresh one. In selected experiments investigating neurites, N2A-P1KO cells were serum-starved for approximately 12h to promote neurite outgrowth. Cells are then used within 24h to 48h.

For hypo-osmotic experiments, cells were washed once with PBS, then incubated for 3min at 37°C in a 120mOsm Ringer's solution (48.8mM NaCl, 5mM KCl, 10mM HEPES, 10mM

glucose, pH 7.4) and finally fixed for 15min at room temperature in a hypotonic fixative (0.5% PFA, 0.05% glutaraldehyde, 200mOsm). For cytochalasin D (Sigma) experiments, cells were incubated for 20min at 37°C with 2μM cytochalasin D diluted in culture medium, which was kept after in the fixative solution (Minflux imaging) or in the extracellular buffer (electrophysiology).

Electrophysiology

All PIEZO constructs generated were tested for proper functionality in patch-clamp assays and compared to control PIEZO1-IRES-GFP. Mechanically activated currents were recorded at room temperature using EPC10 amplifier with Patchmaster software (HEKA Elektronik). Borosilicate patch pipettes (2–6 MΩ for whole-cell, 1.5–3.5 MΩ after fire-polishing for cell-attach) were pulled with a P-97 Flaming-Brown puller (Sutter Instrument). For whole-cell patch clamp, intracellular buffer contained the following: 125mM K-gluconate, 7mM KCl, 1mM $MgCl_2$, 1mM $CaCl_2$, 4mM EGTA, 10mM HEPES (pH 7.3 with KOH). For single-channel cell-attach: 130mM NaCl, 5mM KCl, 1mM $MgCl_2$, 1mM $CaCl_2$, 10mM HEPES, 10mM TEA-Cl (pH7.3 with NaOH). The control bath solution for whole-cell contained the following: 140mM NaCl, 4mM KCl, 1mM $MgCl_2$, 2mM $CaCl_2$, 4mM glucose and 10mM HEPES (pH 7.4 with NaOH). For single channel recordings, the bath solution contained: 140mM KCl, 1mM $MgCl_2$, 2 $CaCl_2$, 10 Glucose, 10 HEPES (pH7.4 with KOH). Cells were held at a holding potential of -60 mV (whole-cell and cell-attach).

Mechanical stimulation in whole-cell experiments was done with a series of 15 mechanical stimuli in 0.6 μm increments with a fire-polished glass pipette (tip diameter 2-3μm) that was positioned opposite to the recording pipette, at an angle of approximately 45° to the surface of the dish and moved with a velocity of 1 μm/ms by a piezo driven micromanipulator (Preloaded Piezo actuator P-840.20, Physik Instrumente). Negative pressure stimuli in cell-attach experiments were applied for 500ms with the High-Speed Pressure Clamp device (HSPC; ALA Scientific Instruments), with -5mmHg increments up to -80mmHg. A pre-pulse of +5mmHg was applied before negative-pressure stimuli to improve recovery from inactivation[51]. For I/V experiments, pressure stimulus was adjusted on a cell-by-cell basis to optimally evoke single-channel openings.

The evoked whole cell currents were recorded with a sampling frequency of 200 kHz and filtered with 2.9 kHz low-pass filter. Pipette and membrane capacitance were compensated using the auto function of Patchmaster. Recordings with excessive leak currents, unstable access resistance and cells which giga-seals did not withstand at least 7 consecutive mechanical steps stimulation were excluded from analyses. Mechanical thresholds of PIEZO currents were determined by measuring the mechanical stimulus that evoked the first sizeable peak current, defined as the point in which the current significantly differed from the baseline

(more than 6 times the standard deviation of the baseline). The inactivation time constants (τ_{inact}) were measured by fitting the mechanically activated currents with a single exponential function ($C1+C2*e^{(-(t-t0)/\tau inact)}$, where C1 and C2 are constants, *t* is time and τ_{inact} is the inactivation time constant. For each cell, only peak currents between 100pA and 1500pA were used for τ_{inact} calculation and averaged from cell to cell.

The evoked cell-attach currents were recorded with a sampling frequency of 50 kHz and filter with a 2.9 kHz low-pass filter. Maximal pressure-evoked currents over the course of a given stimulus (I) were normalized to the absolute maximal response of the cell at any pressure (I_{max}). Normalized pressure-response curve (I/I_{max}) from individual cells were fitted with a Boltzmann sigmoid to determine individual P50 (in mmHg).

Single-channel amplitudes at a given holding potential (-140mV to -40mV, 20mV steps) were determined as the difference between the peaks of the gaussian fits of the trace histogram over multiple 1s segments. Unitary conductance was determined from the linear regression fits of the I/V plot of individual cells. Recordings with excessive leak currents or unstable baseline were excluded. Recordings that displayed non-inactivating responses or unstable openings were also not used for further I/V analyses.

Preparation of samples for TIRF imaging

For lived samples, N2A-P1KO cells were plated on glass bottom dishes as described before and transfected with PIEZO1-ALFA-mGL. Two to three days after transfection, samples were processed for live imaging. For fixed samples, N2A-P1KO cells were plated on 18mm coverslips and transfected with PIEZO1-ALFA-mGL. Two to three days after transfection, cells were washed once with PBS and fixed for 10min at room temperature with a mixture of 1% PFA and 0.1% glutaraldehyde in PBS. Fixative was removed and quenched with 5mM $NaBH_4$ in PBS (one quick wash and another one for 5min at room temperature) and then with 50mM glycine and 50mM NH_4Cl in PBS (one quick wash and another one for 5min at room temperature). Samples were further washed thrice with PBS for 5min at room temperature. Cells were then blocked with either a mix of 5% FBS, 1% BSA in PBS (No permeabilization) or with additionally 0.2% Triton 100X and 0.05% Tween 20 (Permeabilization) for 30min at room temperature. Samples were then labelled with a nanobody against ALFA tag conjugated with Alexa-647 (FluoTag-X2 anti-ALFA, NanoTag Biotechnologies) diluted 1:100 into respective blocking buffers and incubated for 1 hour at room temperature. Samples were then washed 3 times for 5min at room temperature with their respective blocking buffers. A post-fixation step was then performed, using the same fixative mixture as before, for 5min. Fixatives were quenched and then washed 3 more times with PBS. Coverslips were then mounted on slides with ProLong Glass Antifade Mountant (ThermoFisher). Samples were then imaged within 2 days.

TIRF microscopy imaging and acquisition

TIRF imaging was performed on a Nikon Eclipse TiE microscope and with a Roper iLAS2 TIRF module. The objective was an oil immersion Nikon CFI Plan Apo Lambda 100x (NA 1.45) and the camera used was a Photometrics Prime 95B back-illuminated sCMOS, having a resolution of 1200 x 1200 and with a pixel size of 11 µm. A 1.5x magnification lens was added, giving a final pixel size of 0.073µm. Cells were illuminated with solid-state lasers of 488nm and 640nm (20% power for both). Acquisition was done with VisiView software (version 5.0.0, Visitron Systems). For live imaging, cells were imaged for 30s with a frame rate of 10Hz (approximately 100ms exposure time per frame). An incubation chamber (okolab) was used to adjust temperature (37°C), CO2-concentration (5%) and humidity.

TIRF microscopy analysis

Clusters and tracks analysis from live-imaging were processed as described before[21,48]. Time-lapse recordings were first preprocessed in ImageJ with a bleach correction (Histrogram matching, [52]). PIEZO track analysis was then performed with TrackMate v7.13.2 [53,54] and the following parameters: DoG detector, blob diameter of 0.35µm, spots quality filter value of 0.30-1, simple LAP tracker with a linking distance of 0.7µm, a gap closing distance of 0.7µm and a maximal gap closing frame number of 2. Only tracks that have a duration of at least 40 frames were considered for further analysis. Tracks classification was done in ImageJ with the TraJClassifier plugin [55] and the following parameters: minimal track length 40, window size 30, minimal segment length 30. MSD calculation and subsequent analysis were then performed in Matlab using custom scripts (Mathworks). To simplify classification, the classes “Subdiffusion” and “Confined” were labelled as “Immobile”, and “Directed” and “Normal diffusion” as “Mobile”.

For fixed samples, analysis was performed in ImageJ. PIEZO clusters were identified on the mGL signal (488nm excitation): a background subtraction (rolling ball radius 5) was first performed, a Gaussian blur was applied (sigma 2 and 3) and blurred images were subtracted. An Auto-local Threshold was then used (Bernsen method, radius 5) followed by a Particle Detection (min. size = 10 and max. size =50 pixels) to identify clusters as Region of Interests (ROIs). Intensity of the mGL and ALFA-Alexa647 signals were then measured within the ROIs and mGL clusters were classified or not as ALFA-Alexa647 positive.

Preparation of samples for DNA-PAINT Minflux imaging

N2A-P1KO cells were plated on 18mm coverslips as described in previous section and transfected with PIEZO1-mGL, PIEZO1-ALFA-HA or PIEZO1-ALFA-mGL. Two to three days after transfection, cells were processed for fixation as described above for TIRF imaging or

first treated with hypotonic solution or cytochalasin D and then fixed as described above. After quenching and washing of fixatives, samples were blocked with Antibody Incubation buffer (Massive Photonics) for 30min at room temperature. The cells were incubated for 1h at room temperature or overnight at 4°C with Massive-Tag-Q Anti-ALFA or Anti-GFP nanobodies conjugated with a DNA docking strand (both from Massive Photonics) diluted at 1:100 (Anti-ALFA) or 1:200 (Anti-GFP) in Antibody Incubation buffer. PIEZO1-ALFA-HA samples were fixed, blocked and permeabilised as described above for TIRF samples, then incubated with the anti-GFP nanobody and with a rabbit anti-HA antibody (1:500, ThermoFisher). Cells were washed thrice with 1X Washing buffer (Massive Photonics) and then post-fixed for 5min. Fixatives were quenched and washed as described before. PIEZO1-ALFA-HA samples were then incubated for 1 hour with a secondary antibody donkey anti-rabbit coupled to Alexa488 (Life technologies), and further washed with PBS. Samples were then incubated for 10 min with 100-200 µl of gold nanoparticles for future stabilization (gold colloid 250nm, BBI Solutions, or A12-40-980-CTAB, Nanopartz). Unbound nanoparticles were rinsed extensively with PBS and remaining nanoparticles were further stabilized with PLL for at least 1hr at room temperature. Cells were then washed thrice with PBS before mounting. Labelled samples were used within 3 days. DNA-PAINT imagers (Massive Photonics) conjugated to Atto 655 were freshly diluted in Imaging buffer (Massive Photonics) for a final concentration of 1 ~ 2nM (Atto 655 and ALFA imaging, Imager #3) or 1nM (Atto655 and GFP imaging, Imager #2). A drop of imager dilution was added into a cavity slide and coverslips were mounted and sealed with picodent twinsil (picodent).

3D Minflux imaging

Minflux imaging was performed on an Abberior MINFLUX commercial microscope built on an inverted IX83 microscope with a 100X UPlanXApo objective (Olympus) and using Imspector Software (Abberior Instruments). Daily alignment and calibration of the excitation beam pattern and position of the pinhole was performed using fluorescent nanoparticles (abberior Nanoparticles, Gold 150 nm, 2C Fluor 120 nm, Abberior Instruments). Cells were identified with a 488nm confocal scan and the transient binding of imagers with Atto655 was quickly verified with 640 nm confocal scan. At least 2 gold fiducials were present in the field of view and used by the active-feedback stabilization system of the microscope (IR 975nm laser, Cobolt, and CCD camera, The Imaging Source), having typically a precision below 1nm in all three axes and being stabled for hours, enabling overnight acquisition. A ROI of 1x1 to 4x4 µm (up to 8x8 µm for some overnight recordings) was selected at the cell-coverslip interface, except for some neurites where focus was set approximately in their middle height. Laser power in the first iteration and pinhole were set at 16% laser power and 0.83 A.U pinhole. Final laser power in the last iteration is scaled up by a factor of six. ROIs were imaged for at least 2

hours and up to overnight (~12 hours) using the standard 3D Minflux sequence (Extended Data Table 1). Detection for Atto 655 signals was performed with two avalanche photodiodes channels (650-685nm and 685-720nm) that were pooled. Specificity of the nanobodies and imagers used in this study and of the Minflux signal was tested by incubating samples transfected with PIEZO1-mGL with the anti ALFA nanobody and samples transfected with PIEZO1-ALFA-HA with the anti GFP nanobody (Extended Data Fig. 2b and 7b and c).

Minflux data analysis

Final valid localizations from Minflux iterations were exported from Imspector software as matlab files. Custom Matlab scripts were then used for post-processing and filtering of the data, as well as subsequent operations and data visualization. Data filtering involved first an efo filter (effective frequency at offset, kHz, retrieved for each individual valid locations) based on its overall distribution for each individual measurements: a threshold was then selected to filter-out potential multiple emitters. An additional cfr filter was used for mGL/GFP cluster experiments, with a cutoff value of 0.5 (0.8 elsewhere, directly implemented during the acquisition). Then, localizations from the same emission trace, i.e. with the same trace identification number (TID), having a standard deviation of more than 10 nm in the x, y, z axes and less than 6 localizations were excluded (see Extended Data Fig. 2c and 7d). For ALFA signals, filtered traces were trimmed of their first 2 localizations, as they are often apart from the rest and the majority of the localization cloud, possibly caused by diffusing imager molecules. For GFP signals, localizations for each trace were aggregated (group of 3), as described elsewhere [38]. Remaining traces were further corrected for the refractive index mismatch between the coverslip and the sample, applying a scaling factor of 0.7 for all traces in the z dimension [35].

For mGL/GFP cluster experiments (Fig.1 and 2), clusters were manually selected and analysed as follows. The center of mass of each individual filtered trace (i.e trace with the same TID) within the clusters was calculated. Due to the nature of DNA-PAINT labelling and the proximity of individual mGL molecules at PIEZO C-ter, neighbouring signals coming from the same PIEZO channel were estimated and averaged using a DBSCAN on the trace average calculated before, with a minPoints of 2 and epsilon of 25nm (based on recording precision and labelling error), ultimately giving a position of an individual PIEZO channel (See Extended Data Fig. 2c and d). To classify clusters into pit-shaped (open at the top) and spherical clusters, we segmented the raw MINFLUX localization data of each cluster into signals originating from the upper fifth (top) and the lower four fifth (bottom) (Fig. 1d), and classified clusters in which no channels were present near the center of the top segment (i.e. within a distance of 0.25 times the radius from the centroid), as pit-shaped clusters, whereas those clusters that did contain channels in this region were considered as spherical clusters

(Fig. 1e). To estimate the local curvature of the membrane at the position of individual PIEZO1 channels within cluster, we fitted the 3D distribution of the trace means using a modified 2D Gaussian distribution that contained a term correcting for cluster width, Z = top + depth – depth/(1+e^((2*width^2 – ((X – CenterX)^2) – ((Y – CenterY)^2))/slope^2)), where X, Y, Z are the coordinates of the channels, CenterX and CenterY are the arithmetic means of the X and Y coordinates of all channels. For surface fitting 'top' (Z-coordinate of the topmost channel) and 'depth' (distance between the topmost and the lowest channel) were held constant and the width and slope of the clusters were fitted using the custom fit fuciton in IgorPro v8.04. The gaussian curvatures at the coordinates of the channels were then calculated using a custom written script in Matlab (see code availablity).

For ALFA trimer experiments, signals were filtered and the center of mass of each individual trace was calculated. Traces originating from repeated detection of the same protomer, were identified using DBSCAN clustering with minPoints of 2 and epsilon of 8 nm. The 8 nm cutoff was chosen based on the localisation precision of MINFLUX and the possible ALFA-tag flexibility (Extended Data Fig. 3a). The position of the protomers that were detected multiple times, was determined by calculating the mean coordinate of the localisations clustered by the DBSCAN algorithm. PIEZO1 trimers in which all three protomers were labelled and detected by MINFLUX were identified by searching for three adjacent traces that were less than 40 nm apart, which we assumed is the maximum distance two Atto-655 molecules bound to the same PIEZO1 trimer can possibly have, and that had no other neighboring traces within a distance of 60 nm (Extended Data Fig. 8a). Moreover, only trimers in which the maximum interblade angle was smaller than 120° were considered.

Structure modelling and data visualization

Due to the similar topology and overall structure similarity between PIEZO1 and PIEZO2, the cryo-EM structure model of full-length PIEZO2 trimer (PDB 6KG7) was used only for display purposes, showing the relative position of the ALFA tag at the N-ter of the blade and of the mGL at the C-ter, with their respective nanobody (PDB 6I2G for ALFA, PDB 3K1K for mGL/GFP). All subsequent modification operations and visualization were performed in PyMol (version 2.5.5, Schrodinger). Plasmid design and visualization was performed with SnapGene (version 7, Dotmatics). All the other data, graphics and schematics were elaborated and visualized in Matlab, Illustrator (Adobe) and GraphPad Prism (version 10, GraphPad Software).

Statistical tests and reproducibility

All experiments in this study were performed independently at least three times, yielding similar results. No statistical method was used to predetermine sample size. Experiments were not randomized and investigators were not blinded during experiments and analysis. Data distribution was systematically evaluated using D'Agostino–Pearson test and parametric or non-parametric tests were chosen accordingly. The statistical tests that were used, the exact P-values and information about the number of replicates are provided in the display items or the corresponding figure legends.

Reporting summary

Further information on research design is available in the Nature Portfolio Reporting Summary linked to this article.

Data availability

All data supporting the article, such as the MINFLUX and patch-clamp analysis outputs for each experimental condition, are provided as source data. Raw data and reagents that are not commercially available are available from the corresponding author upon reasonable request. Source data are provided with this paper.

Code availability

The custom Matlab codes for Minflux analysis are available at https://github.com/clementverkest/PIEZO1_MinfluxAnalysis. The custom Matlab code for PIEZO tracks, Trackmate and TraJClassifier output analysis is available at https://github.com/clementverkest/PIEZO_Track_Analysis.

Methods references

48. Schaefer, I. *et al.* PKA mediates modality-specific modulation of the mechanically gated ion channel PIEZO2. *J Biol Chem* **299**, 104782 (2023).
49. Campbell, B. C. *et al.* mGreenLantern: a bright monomeric fluorescent protein with rapid expression and cell filling properties for neuronal imaging. *Proc Natl Acad Sci U S A* **117**, 30710–30721 (2020).
50. Götzke, H. *et al.* The ALFA-tag is a highly versatile tool for nanobody-based bioscience applications. *Nat Commun* **10**, 4403 (2019).
51. Lewis, A. H. & Grandl, J. Mechanical sensitivity of Piezo1 ion channels can be tuned by cellular membrane tension. *eLife Sciences* **4**, e12088 (2015).
52. Miura, K. Bleach correction ImageJ plugin for compensating the photobleaching of time-lapse sequences. Preprint at https://doi.org/10.12688/f1000research.27171.1 (2020).

53. Ershov, D. *et al.* TrackMate 7: integrating state-of-the-art segmentation algorithms into tracking pipelines. *Nat Methods* **19**, 829–832 (2022).
54. Tinevez, J.-Y. *et al.* TrackMate: An open and extensible platform for single-particle tracking. *Methods* **115**, 80–90 (2017).
55. Wagner, T., Kroll, A., Haramagatti, C. R., Lipinski, H.-G. & Wiemann, M. Classification and Segmentation of Nanoparticle Diffusion Trajectories in Cellular Micro Environments. *PLOS ONE* **12**, e0170165 (2017).
56. Taberner, F. J. *et al.* Structure-guided examination of the mechanogating mechanism of PIEZO2. *Proc. Natl. Acad. Sci. U.S.A.* **116**, 14260–14269 (2019).

Acknowledgements

We thank Dr. Antonio Failla and the team of the imaging core facility at UKE Hamburg (DFG Research Infrastructure Portal #RI_00489) for technical assistance with the MINFLUX microscope. Funding for the MINFLUX microscope was awared by the the Hamburgische Investitions- und Förderbank (IFB, grant no. 51164232) under the Operational Programme Hamburg ERDF 2014-2020, REACT-EU of the European Regional Development Fund (ERDF). We also thank Mr. Haider Al-Marsoomi and Ms. Claudia Lüchau for assistance with cloning and cell culture. This work was funded by the DFG grant LE3210/3-3 awarded to S.G.L.

Author contributions

C.V. performed all imaging and patch clamp experiments, wrote code and analyzed the data. L.R. performed patch-clamp experiments and wrote analysis code. N.Z. performed patch-clamp experiments. S.G.L. conceptualized the study, acquired funding, wrote analysis codes, analyzed data and wrote the manuscript.

Competing interests

The authors declare no competing interests

Figures 1 – 4

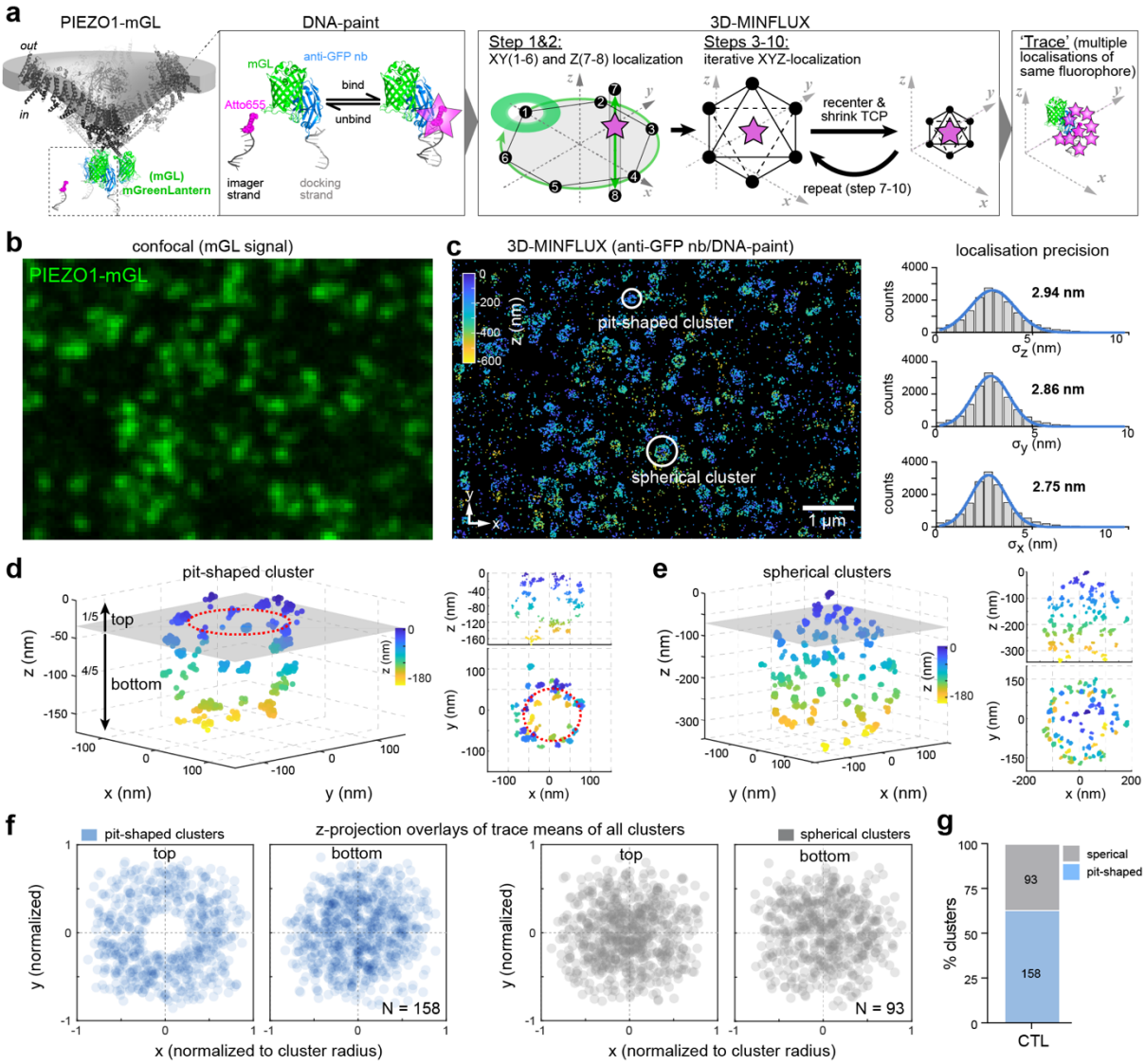

Fig. 1, 3D-MINFLUX reveals pit-shaped nanoarchitecture of PIEZO1 clusters

a, cryo-EM structure of PIEZO and localization of mGreenLantern(mGL)-tag (left) and cartoon illustrating the principle of MINFLUX/DNA-PAINT (right). DNA-PAINT utilizes complementary pairs of short oligonucleotides, an imager strand conjugated to the fluorophore and a docking strand conjugated to an sd-Nb that binds to the target. To determine the fluorophore position, the MINFLUX microscope performs an iterative 3D scanning procedure, which is repeated until the fluorophore is bleached or the imager strand dissociates from the target, such that 'traces' with multiple localization estimates of the same fluorophore are generated. **b**, shows a confocal scan of an N2a cell expressing PIEZO1-mGL and **c**, shows the corresponding MINFLUX localization data (left) and the distribution of the standard deviations of the MINFLUX traces along the x, y, and z-axis (right) **d** and **e**, show 3D-views, top views and side views of the raw MINFLUX localization data of the pit-shaped (d) and the spherical (e) clusters marked in **c**. For 360° rotation movies of the clusters shown in d and e, see Supplementary Video 1 and 2. **f**, Overlay of the 2D projections of the traces means of the top fifth and bottom four fifth of all pit-shaped clusters (blue circles, N=158 cluster from 19 cells) and spherical clusters (grey circles, N=93 clusters from 19 cells). Note, in pit-shaped clusters no channels are present at the center of the top fifth. **g**, bar graph showing the proportions of pit-shaped and spherical clusters.

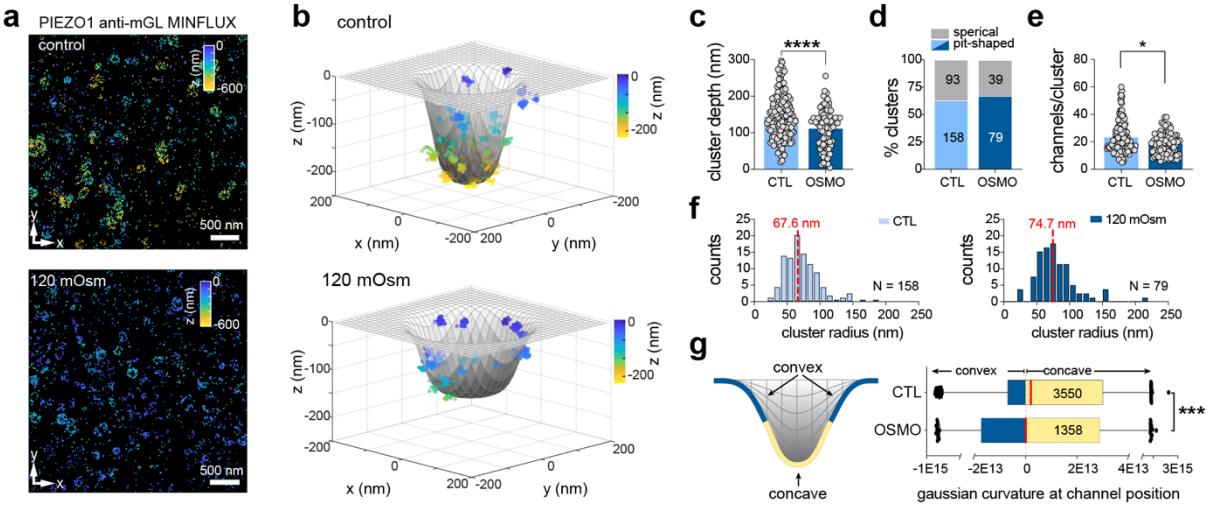

Fig. 2, Hypo-osmotic stimulation causes partial flattening of pit-shaped clusters
a, raw MINFLUX localization data color coded by Z-position of clusters imaged in control cells (top) and cells challenged with hypoosmotic solution (120 mOsm) before fixation (bottom). **b**, 3D-views, of the raw MINFLUX localization data of representative clusters from control (top) and osmotically stimulated (bottom) cells together with surface fits. For 360° rotation movies of the clusters see Supplementary Video 4-5. **c**, comparison of the cluster depths of control and hypo-osmotically stimulated cells (CTL: 144 ± 60 nm, N=158 vs. OSMO: 110.7 ± 54 nm, N=79, P=0.000052, two-tailed Student's t-test). **d**, comparison of the proportions of pit-shaped (blue) and spherical clusters (grey) in control (CTL) and hypo-osmotically stimulated (OSMO) cells. The numbers provided in the bars represent the absolute number of clusters from the two categories. **e**, comparison of the mean ± sem number of PIEZO1 channel found in pit-shaped clusters. Circles represent the number of channels in individual clusters (CTL: 23.1±11.3, N=158 vs. OSMO: 18.7±8.0, N=79, P=0.0134, two-tailed Mann-Whitney test). **f**, histograms showing the distribution of the radii of all pit-shaped clusters measured at the pit opening. Medians are indicated by the red dashed lines. **g**, the left panel shows the side view of an example surface fit in which the contours of convex regions are depicted in blue and the contours of concave regions are shown in yellow. Gaussian curvatures of the fitted surfaces (see b) at the coordinates where channels were detected, were calculated and are shown as horizontal box plots. Boxes range from the lower quartile to the upper quartile, medians are shown as red lines and negative and positive curvatures are color coded in blue and yellow, respectively. Mean curvatures were compared using non-parametric Mann Whitney test (***, P = 0.0004, N=3550 for CTL and N=1358 for OSMO).

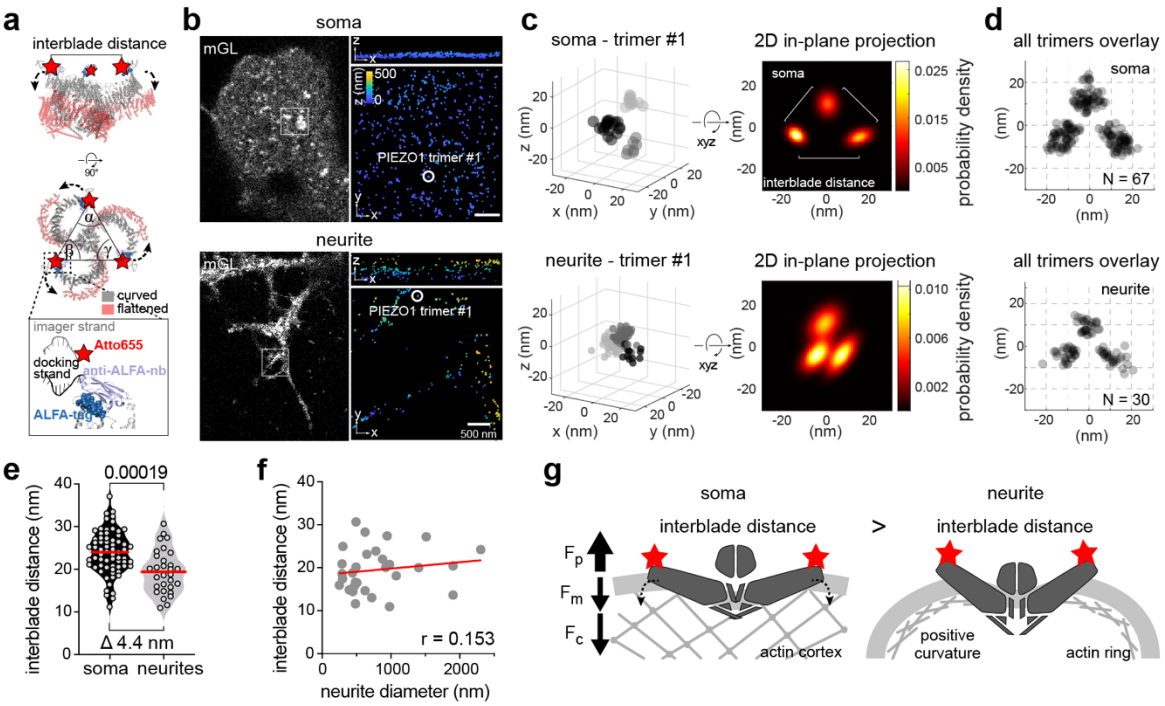

Fig. 3, PIEZO1 is more contracted in neurites as compared to the cell soma

a, side and top views of PIEZO, in the curved (grey) and flattened (red) conformation. Distances between ALFA-tags from one trimer are designated as 'interblade distance' and the angles between the lines connecting the ALFA-tags (α,β,γ) as 'interblade angles'. **b**, confocal image of an N2a cell expressing PIEZO1-ALFA-mGL (left) and top and side view of the corresponding MINFLUX localization data from the marked regions in the soma and neurites (Supplementary Video 6 for 360° rotation movies of the example shown here and Supplementary Video 7-10 for additional examples). **c**, 3D scatter plot of raw localizations of representative trimers found in a cell soma (top-left) and in a neurite (bottom-left). Localizations originating from fluorophores bound to different protomers are colored in black, dark grey and light grey. The 3D raw localizations were projected vertically onto the plane defined by the trace means (2D in-plane projection) and then fitted with a bivariate Gaussian distribution. The heatmaps in the right column show the probability densities of the Gaussian distributions. **d**, superparticle of all trimers found in somata (top) and in neurites (bottom), generated by aligning the trace means of each identified trimer to a reference trimer (equilateral triangle with a side length of 25nm) using the iterative closest point algorithm of Matlab. **e**, comparison of the mean ± sem interblade distances of trimers residing in somata (black bar, N=67 trimers from 10 cells) and neurites (grey bar, N=30 trimers from 10 cells) using two-tailed Students t-test (P=0.00019). Values from individual trimers are shown as grey circles. **f**, Interblade distance are plotted against neurite diameter, showing that there is no correlation between the two parameters (Pearson coefficient r = 0.153). **g**, cartoon showing the lack of an effect of membrane curvature on PIEZO1 conformation and highlighting differences in cytoskeletal architecture of somata and neurites.

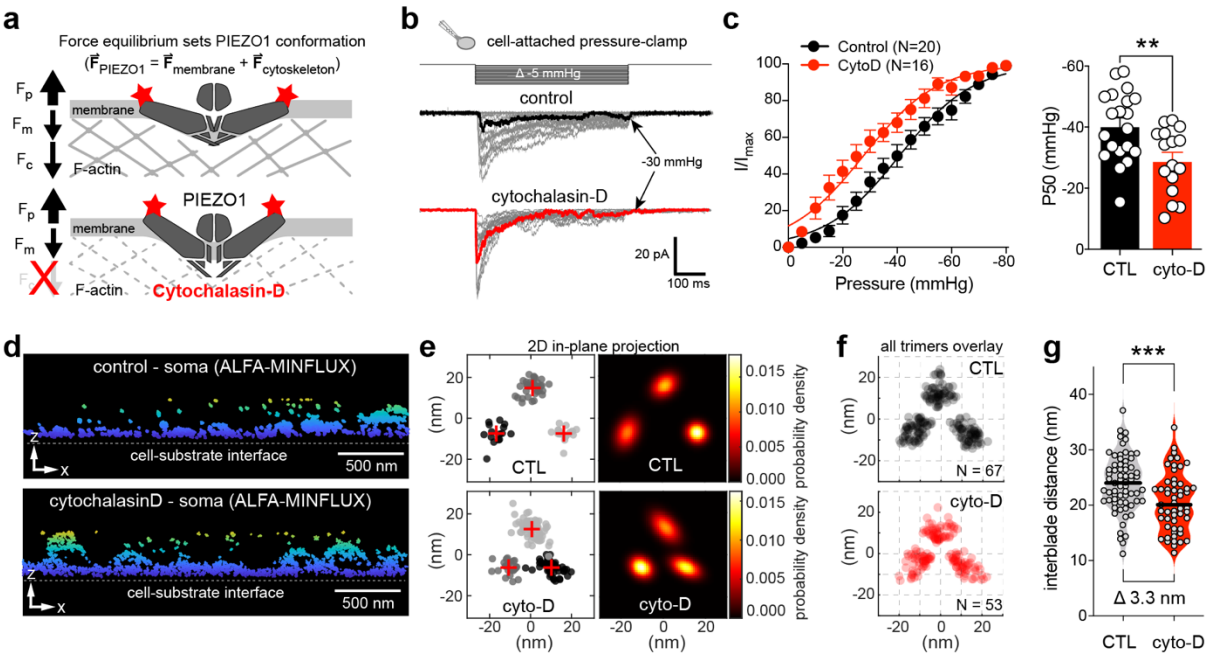

Fig. 4, Disruption of the cytoskeleton alters PIEZO1 conformation

a, cartoon showing the possible interplay of forces. PIEZO1 exerts a bending force onto the membrane (F_{PIEZO1}, F_p) while the membrane ($F_{membrane}$, F_m) and the cytoskeleton ($F_{cytoskeleton}$, F_c) exert opposing forces on PIEZO1, which work towards opening the channel. We hypothesize that the equilibrium of these forces eventually determines PIEZO1 conformation. The bottom panel illustrates the effect of cytochalasin-D on the actin cortex and the resulting change in the force equilibrium. **b**, example traces of PIEZO1-mediated currents evoked by negative pressure in cell-attached patch-clamp recordings. **c**, left panel shows normalized (I/Imax) pressure-response curves of PIEZO1 currents recorded from control (black circles) and cyto-D treated (red circles) cells (left panel). Comparison of the mean ± sem P50 values (P50 = pressure required for half-maximal activation, right panel) obtained by Boltzmann fits of the data shown in the left panel, using Student's t-test (CTL: p50 = -40.6 ± 2.5 mmHg, N=20 vs. cyto-D: p50 = -29.1 ± 2.6 mmHg, N =16; P = 0.0038). White circles show P50 values from individual recordings. **d**, side views of MINFLUX raw localization data from a control (top) and a cyto-D-treated cell. Note, cyto-D treatment does not change the curvature of the cell-substrate interface. **e**, 2-D in-plane projections of the raw localization data (left) and heatmaps of the localization probability densities (right) of representative trimers from control (CTL, top) and cyto-D (bottom) treated cells. **f**, superparticle of all trimers found in control (CTL, top) and cyto-D (bottom) treated cells (see description in Fig. 3). **g**, comparison of the mean ± sem interblade distances of all trimers from control (23.90 ± 5.14 nm, N=67, grey) and cyto-D (20.58 ± 5.30, N=53, red) treated cells using Students t-test (P=0.0007). Values from individual trimers are shown as grey circles.